Passivity-Based Control Design Methodology for UPS Systems

Rymarski, Zbigniew ; Bernacki , Krzysztof ; Dyga , Łukasz ; Davari, Pooya

Published in:
Energies

DOI (link to publication from Publisher):
10.3390/en12224301

Publication date:
2019

Document Version
Publisher's PDF, also known as Version of record

energies

MDPI

Article

Passivity-Based Control Design Methodology for UPS Systems

Zbigniew Rymarski [1,*], Krzysztof Bernacki [1], Łukasz Dyga [1] and Pooya Davari [2]

[1] Institute of Electronics, Faculty of Automatic Control, Electronics and Computer Science, Silesian University of Technology, Akademicka 16, 44-100 Gliwice, Poland; krzysztof.bernacki@polsl.pl (K.B.); lukasz.dyga@polsl.pl (Ł.D.)

[2] Department of Energy Technology, Aalborg University, DK-9220 Aalborg, Denmark; pda@et.aau.dk

* Correspondence: zbigniew.rymarski@polsl.pl

Received: 11 October 2019; Accepted: 9 November 2019; Published: 11 November 2019

Abstract: This paper presents a passivity-based control (PBC) design methodology for three-phase voltage source inverters (VSI) for uninterruptable power supply (UPS) systems where reduced harmonic distortions for the nonlinear load, reduced output voltage overshoot, and a restricted settling time are required. The output filter design and modification for efficient control and existing challenges with the assignment of scaling coefficients of the output voltage, load, and inductor currents are addressed and analyzed. Notably, special attention is given to the modulator saturation issue through implementing an accurate converter model. Applications of the two versions of PBC in three-phase voltage source inverters using stationary $\alpha\beta$ and rotating dq frames for a constant frequency of the output voltage are presented. Furthermore, the influence of the PBC parameters on the power converter performance is investigated. A comparative simulation and the experimental results validate the effectiveness of the presented passivity-based control design methodology.

Keywords: control systems; state space models; voltage source inverters; power conversion systems; PBC control

1. Introduction

The control design of single-phase and three-phase voltage source inverters (VSI) for uninterruptable power supply (UPS) systems has been extensively discussed for the last four decades [1–6]. The PBC control strategies are implemented in renewable energy sources and energy storage systems [7]. Typically, two control types for the UPS systems are implemented in order to meet the standard requirements that are defined by IEC 62040-3 [8] for nonlinear rectifier resistive-capacitive (RC) load types. The first one is based on the single input single output (SISO) approach where only the output voltage is measured and controlled, while in the second approach, a multi input single output (MISO) controller is employed to regulate the output voltage based on the output current, inductor current, and the output voltage measurements. A proportional–integral–derivative controller (PID) is a standard SISO control (e.g., designed based on the quasi-continuous transfer function [9]). The other PID-like controller is based on the coefficient diagram method (CDM) [10]. The results of such a control can be satisfactory but treating the current as an unmeasured disturbance can lead to higher distortions of the output voltage than in the case of a MISO controller. Very good results can be obtained with a SISO controller using a plug-in repetitive controller (RPC) in the outer negative feedback loop, which works as a harmonics generator [3]. We designed an RPC using the zero phase error tracking compensation (ZPETC) technique [11]. The plug-in zero phase repetitive controller can be designed quite simply for a CDM controller in the inner control loop of an inverter [12]. However, an RPC has one serious disadvantage—it remembers the whole previous fundamental period (in some solutions

only half of it [3]). Therefore, when the harmonic disturbances vanish, the RPC has a fault response on the non-existent disturbance [12]. The MISO approach generally results in lower distortions of the output voltage for all types of disturbances as well as a higher robustness. Commonly, the load current is treated as an independent current source disturbance, thus making the inverter model independent of the load. However, since this method ignores the interaction of the inverter output voltage and the load current, it may not guarantee the required performance of a UPS system over a wide range of operating conditions that can change the location of the roots of the characteristic polynomial of a closed loop system [12]. In the recent years, the passivity-based control (PBC) approach that was introduced by Ortega [13] in 1989 and further extended in [14–18] has been employed for VSI. PBC is based on a MISO control and it is a suitable candidate for power conversion systems control (e.g., VSI) and has been widely used in induction motor drive systems [19,20]. When using PBC, a converter is treated as an "energy transformation multiport device" [21]. The idea of this controller is based on keeping the system behavior passive (i.e., the stored energy is always less than the supplied energy), which also requires "the injection" of proper damping [22]. The advantage of the PBC is the global stability of the controlled system. The choice of the acceptable gains of the controller is flexible and the control system is robust for the inverter parameter changes (parametric uncertainty) [22–24]. This paper proposes a PBC-based design methodology for three-phase inverters and presents a comparison of their control [25] using stationary $\alpha\beta$ and rotating dq frames. In order to further improve the conventional PBC performance, proper output filter design as well as advanced PBC techniques that follow the IEC 62040-3 [8] and IEEE-519 [26] standard requirements will be considered. Notably, special attention is given to the modulator and controller saturation issues during dynamic loading. Thereby, the main aim of this paper is to provide guidelines and a design methodology on how to apply the simplest PBC approach for a three-phase VSI (simpler than e.g., the Interconnection and Damping Assignment Passivity-Based Control (IDA–PBC) idea presented in [27]) while maintaining a reasonable compromise between the ideal theory and the customer demands (with the more enhanced direct control of the output voltage than presented in [22]). The results of the modulator saturation effect, the problem of the restriction of the modulation index, the problem of the influence of the scaling factors in the measuring tracks on the PBC controller gains, and the final adjustment of the controller gains to reach the lowest distortions of the output voltage for the standard loads were not discussed yet [27–29]. The aim of the paper is to present a PBC version that can be easily implemented in a standard modern microcontroller delivering the pulse width modulation (PWM) signal with the acceptable high switching frequency. The presented difference control laws of PBC are devoted to this.

This paper is structured as follows. Section 2 describes the output filter sizing and selection. The state space modeling of an inverter in the stationary and rotating frames is presented in Section 3. Section 4 is dedicated to the design of different PBC. In Section 5, simulation and experimental results are provided to substantiate the effectiveness of the proposed design methodology for two versions of PBC. Finally, after the results and discussion, conclusions are drawn in Section 8.

2. The Output Filter Parameters

The basic approach to VSI design begins with the L_fC_f output filter design. The design should ensure a sufficiently low ripple voltage amplitude (IEC 62040-3 [8], IEEE519 [26]) and the total harmonic distortion of the output voltage (THD_V) level for static linear and nonlinear rectifier RC (R_{load}, C_{load}) loads. These calculations should permit the L_fC_f product value to be assigned. A cost function that is the sum of the absolute values of the reactive power in the filter inductor and the capacitor can then be created. The coefficients of both reactive powers that are assigned are equal [30,31]. For a three-wire star balanced load (Figure 1), a two-level PWM (six transistor h-bridge) [31] (n—phase line number, R_{load}—nominal load resistance, f_s—switching frequency, M—modulation index in actual inverters, M is set close to unity):

$$L_f = \sqrt{\frac{1}{M}}\frac{1}{f_s}R_{load},\ C_f > \frac{1}{f_s}\frac{1}{R_{load}}, \tag{1}$$

or a three-wire delta balanced load (Figure 1), 2-level PWM:

$$L_f = \frac{1}{3}\frac{1}{f_s}R_{load},\ C_f > \frac{1}{f_s}\frac{1}{R_{load}} \tag{2}$$

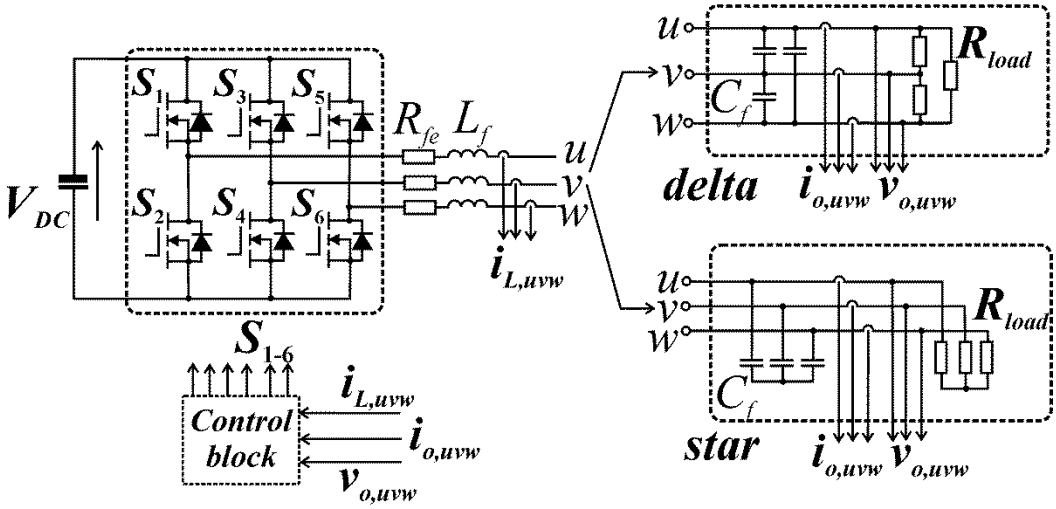

Figure 1. Block diagram of a three-phase voltage source converter with delta and star three-wire load connection.

For example, we assume R_{load} = 43 Ω, f_s = 12,800 Hz, L_f = 1.1 mH, and C_f > 1.8 μF for the delta load. These values are sufficient for reducing the maximum amplitude of the ripple harmonics to 3%. However, for 30 years, researchers of inverter controls have used approximately 50 μF [2,17,24]. The delay of every digital PWM control is at least one switching period. We store the calculated value in the PWM register and in the next switching period the width of the pulses is changed. Let us assume a step load decrease. The inductor works as the current source and most of the excessive inductor current flows through the filter capacitor C_f, thereby increasing the output voltage (e.g., for a one phase for ΔI_{load} = 5 A, switching period T_s = 78 μs for switching frequency f_s = 12,800 Hz, for C_f = 2 μF, we will receive the unacceptable voltage pike ΔV_{out} = 195 V, while for C_f = 50 μF—only ΔV_{out} = 7.8 V). Figure 2a shows the problem in an actual three-phase circuit. The delays in the inverter control loop will be longer than one switching period (the delay of the PWM modulator) while the overshoot will be the same as for the open loop circuit. However, the oversized filter capacitor has disadvantages—there is a much higher reactive power in this capacitor and much larger capacitor currents, which increase the power losses in the parasitic serial resistances and the output voltage has a much longer settling time (Figure 2b). The quality of the output voltage control is better for the low modulation index M because of the higher possible increase $(1 - M)V_{DC}$ of the first harmonic of the inverter bridge output voltage. Output voltage control quality is more efficient for lower output filter inductance values [32]. For a nonlinear rectifier RC load, the value of the voltage over the filter inductor should be steeply increased when the rectifier begins to conduct and a pulse current flows to the load capacitor. Hence, the maximum value of M [32] should be limited to approximately Equation (3):

$$M_{\max} < \frac{\sqrt{3}}{2}/\left(\frac{\omega_m L_f}{R_{serial}} + \sqrt{3}/2\right) \tag{3}$$

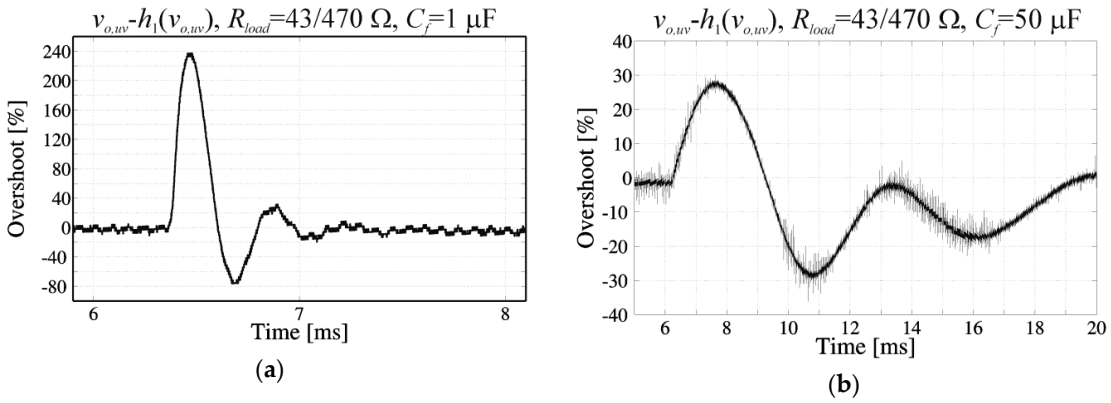

Figure 2. Overshoot and settling time of the output line-to-line voltage $v_{o,uv}$ in the open-loop inverter with (**a**) C_f = 1 μF 1, (**b**) C_f = 50 μF, (f_s = 12,800 Hz, T_s = 78 μs).

M_{max} < 0.65 (too low in practice) for f_m = 50 Hz, L_f = 3 mH, and R_{serial} = 2 Ω is equal to the sum of all of the serial resistances in the load current path when the rectifier conducts including the equivalent series resistance (ESR) of the load capacitor. We used a lower value M = 0.3 in the simulation models and in the breadboard inverter to fully show the advantages of a PBC control. However, this value is too low for market solutions. Sometimes, it is better to permit higher distortions of the output voltage and use a modulation index M close to unity in order to better utilize the input DC voltage (modulation index close to unity leads to higher efficiency of a DC/AC inverter).

3. Initial State Space Models of Three-Phase Inverters in the Stationary $\alpha\beta$ and Rotating dq Frames

The system with delta Δ or star Y loads presented in Figure 1 can be described by the initial (they will be modified further) space equations for small signal space variables in the *abc* frame. The input and output voltages for the star load Y are related to the zero-sequence vector (Equation (4)). In balanced systems, the neutral voltage $v_0 = v_\gamma = 0$.

$$v_0 = v_\gamma = (v_{o,u} + v_{o,v} + v_{o,w})/3 \tag{4}$$

The sinusoidal PWM modulation is preferred for UPS systems (there is a third harmonic of the line to neutral voltages in the space vector modulation (SVM)). The modulated space vector can be presented in the $\alpha\beta\gamma$ coordinates of the stationary frame after using the Clarke [5,33] transformation. For three-wire delta or star loads and for four-wire balanced systems, there is not a zero-sequence vector (γ coordinate) of the used voltage or current variables [34] and the $\alpha\beta$ frame is used. The three-phase voltage or current components are defined as Equation (5).

$$\begin{bmatrix} x_1 & x_2 & x_3 \end{bmatrix}^T = \begin{bmatrix} X_{1m}\cos(\omega t) & X_{2m}\cos(\omega t - 2\pi/3) & X_{3m}\cos(\omega t - 4\pi/3) \end{bmatrix}^T \tag{5}$$

The state space model in the stationary $\alpha\beta$ frame has the advantage of decoupling the models for both axes. Control in the stationary frame has two shifted $\pi/2$ sinusoidal waveforms of the reference voltages. This can be a disadvantage when the reference waveform has a variable frequency. We can use a Park transformation of the stationary $\alpha\beta$ frame and present the space vector in the dq frame rotating with ω_m (angular fundamental frequency of the output voltages). The models for the rotating dq frame are not decoupled (the state variables from one axis influence the other axis variables), which is a disadvantage of this transformation. The problem of decoupling can be solved in the control design [27]. The dq frame is used in the digital motor control of the induction machines. This paper will present the use of both stationary $\alpha\beta$ and rotating dq frames in three-wire, three-phase VSI control

systems. For a delta load (Figure 1), the Clarke transformation and reverse Clarke transformation are Equation (6) [5].

$$\begin{bmatrix} x_\alpha \\ x_\beta \end{bmatrix} = \frac{2}{3}\begin{bmatrix} \frac{1}{2} & 0 & -\frac{1}{2} \\ 0 & \frac{\sqrt{3}}{2} & 0 \end{bmatrix}\begin{bmatrix} x_{12} \\ x_{23} \\ x_{31} \end{bmatrix}, \begin{bmatrix} x_{12} \\ x_{23} \\ x_{31} \end{bmatrix} = \begin{bmatrix} \frac{3}{2} & -\frac{\sqrt{3}}{2} \\ 0 & \sqrt{3} \\ -\frac{3}{2} & -\frac{\sqrt{3}}{2} \end{bmatrix}\begin{bmatrix} x_\alpha \\ x_\beta \end{bmatrix} \tag{6}$$

For a star load (Figure 1), the Clarke transformation and reverse Clarke transformation are Equation (7).

$$\begin{bmatrix} x_\alpha \\ x_\beta \end{bmatrix} = \frac{2}{3}\begin{bmatrix} 1 & -\frac{1}{2} & -\frac{1}{2} \\ 0 & \frac{\sqrt{3}}{2} & -\frac{\sqrt{3}}{2} \end{bmatrix}\begin{bmatrix} x_1 \\ x_2 \\ x_3 \end{bmatrix}, \begin{bmatrix} x_1 \\ x_2 \\ x_3 \end{bmatrix} = \begin{bmatrix} 1 & 0 \\ -\frac{1}{2} & \frac{\sqrt{3}}{2} \\ -\frac{1}{2} & -\frac{\sqrt{3}}{2} \end{bmatrix}\begin{bmatrix} x_\alpha \\ x_\beta \end{bmatrix} \tag{7}$$

The vector $\boldsymbol{d}_{\alpha\beta}$ (Equation (8)) of the output line currents is treated as a disturbance vector [27]. The index α, β or d, q means that the description is separate for the α or d and β or q orthogonal axes; the index $\alpha\beta$ or dq means that the description concerns both axes simultaneously, e.g., the vector of disturbance variables $\boldsymbol{d}_{\alpha\beta}$ and variables $d_{\alpha,\beta}$ are Equation (8).

$$\boldsymbol{d}_{\alpha\beta} = \begin{bmatrix} i_{o,\alpha} & i_{o,\beta} \end{bmatrix}^T, d_{\alpha,\beta} = i_{o,\alpha,\beta} \tag{8}$$

The initial type of $\boldsymbol{x}_i$ state vector, and control and output vectors for the delta and star load (m_α, m_β are the control coefficients of α, β voltages) are Equation (9).

$$\boldsymbol{x}_{i,\boldsymbol{\alpha\beta}} = \begin{bmatrix} i_{Lf,\alpha,\beta} & v_{o,\alpha,\beta} \end{bmatrix}^T, u_{\alpha,\beta} = m_{\alpha,\beta}V_{DC}, \boldsymbol{y}_{a,\beta} = v_{OUT\alpha,\beta} \tag{9}$$

The initial state space model of the three-phase inverter (Figure 1) in the stationary $\alpha\beta$ frame is Equation (10). The only difference between the matrices for the delta and star loads is the value of the equivalent filter capacitor C_{fe}: for the delta load $C_{fe} = 3C_f$ and the star load $C_{fe} = C_f$.

$$\dot{\boldsymbol{x}}_{i,\boldsymbol{\alpha\beta}} = \begin{bmatrix} -\frac{R_{fe}}{L_f} & -\frac{1}{L_f} \\ \frac{1}{C_{fe}} & 0 \end{bmatrix}\boldsymbol{x}_{i,\alpha,\beta} + \begin{bmatrix} 0 \\ -\frac{1}{C_{fe}} \end{bmatrix}d_{\alpha,\beta} + \begin{bmatrix} \frac{1}{L_f} \\ 0 \end{bmatrix}u_{\alpha,\beta} \tag{10}$$

The Park transformation and the reverse Park transformation for the balanced load are Equations (11) and (12).

$$\begin{bmatrix} x_d \\ x_q \end{bmatrix} = \begin{bmatrix} \cos\omega_m t & \sin\omega_m t \\ -\sin\omega_m t & \cos\omega_m t \end{bmatrix}\begin{bmatrix} x_\alpha \\ x_\beta \end{bmatrix} \tag{11}$$

$$\begin{bmatrix} x_\alpha \\ x_\beta \end{bmatrix} = \begin{bmatrix} \cos\omega_m t & -\sin\omega_m t \\ \sin\omega_m t & \cos\omega_m t \end{bmatrix}\begin{bmatrix} x_d \\ x_q \end{bmatrix} \tag{12}$$

A balanced system ($X_{1m} = X_{2m} = X_{3m} = X_m$) in the steady state is described by Equation (5) after a Clarke transformation (Equation (6)), $x_\alpha = X_m\cos\omega_m t$, $x_\beta = X_m\sin\omega_m t$, and after a Park transformation (Equation (11)), $x_d = X_m$, $x_q = 0$—two constant values. This is the main advantage of using the dq frame in a power supply system [34]. The other definition of three-phase components in Equation (5) leads to different results. We use the description that concerns both axes simultaneously because the α or d and β or q variables should be included together in Hamiltonian (Equation (16))—they both participate in storing energy in the system. The final definition of the state variables $x_{\alpha\beta,dq}$ (Equations (13)–(15)) is defined in [27]. For all types of PBC control [21], we use the function $H(x)$ (Hamiltonian) of the total energy stored in the system. For the $\alpha\beta$ or dq frames, $H(x)$ is equal to Equation (16).

$$\boldsymbol{x}_{\alpha\beta,dq} = \begin{bmatrix} L_f i_{Lf,\alpha,d} & L_f i_{Lf,\beta,q} & C_{fe}v_{o,\alpha,d} & C_{fe}v_{o,\beta,q} \end{bmatrix}^T = \boldsymbol{P}\begin{bmatrix} i_{Lf,\alpha,d} & i_{Lf,\beta,q} & v_{o,\alpha,d} & v_{o,\beta,q} \end{bmatrix}^T \tag{13}$$

$$\begin{bmatrix} i_{Lf,\alpha,d} & i_{Lf,\beta,q} & v_{o,\alpha,d} & v_{o,\beta,q} \end{bmatrix}^T = \boldsymbol{P}^{-1}\boldsymbol{x}_{\alpha\beta,dq} \tag{14}$$

$$\boldsymbol{P} = \begin{bmatrix} L_f & 0 & 0 & 0 \\ 0 & L_f & 0 & 0 \\ 0 & 0 & C_{fe} & 0 \\ 0 & 0 & 0 & C_{fe} \end{bmatrix}, \boldsymbol{P}^{-1} = \begin{bmatrix} 1/L_f & 0 & 0 & 0 \\ 0 & 1/L_f & 0 & 0 \\ 0 & 0 & 1/C_{fe} & 0 \\ 0 & 0 & 0 & 1/C_{fe} \end{bmatrix} \tag{15}$$

$$H(x_{\alpha\beta,dq}) = \frac{1}{2}(L_f {i_{Lf,\alpha,d}}^2 + L_f {i_{Lf,\beta,q}}^2 + C_{fe} {v_{o,\alpha,d}}^2 + C_{fe} {v_{o,\beta,q}}^2) = \frac{1}{2}{\boldsymbol{x}_{\alpha\beta,dq}}^T \boldsymbol{P}^{-1}\boldsymbol{x}_{\alpha\beta,dq} \tag{16}$$

We can notice that for the $\alpha\beta$ or dq frames:

$$\boldsymbol{P}^{-1}\boldsymbol{x}_{\alpha\beta,dq} = \partial H(\boldsymbol{x}_{\alpha\beta,dq})/\partial(\boldsymbol{x}_{\alpha\beta,dq}) = \begin{bmatrix} i_{Lf,\alpha,d} & i_{Lf,\beta,q} & v_{o,\alpha,d} & v_{o,\beta,q} \end{bmatrix}^T \tag{17}$$

The space Equations (18) are called the "perturbed Port–Hamiltonian model" of a physical system [13–16,21,29,35] for the $\alpha\beta$ or dq frames because we can substitute (17) in (18). The vector of the input variables $\boldsymbol{m}_{\alpha\beta,dq}$ and the vector of disturbance variables $\boldsymbol{d}_{\alpha\beta,dq}$ is Equation (19).

$$\dot{\boldsymbol{x}}_{\alpha\beta,dq} = [\boldsymbol{J}_{\alpha\beta,dq} - \boldsymbol{R}_{\alpha\beta,dq}]\boldsymbol{P}^{-1}\boldsymbol{x}_{\alpha\beta,dq} + \boldsymbol{G}_{\alpha\beta,dq}\boldsymbol{m}_{\alpha\beta,dq} + \boldsymbol{D}_{\alpha\beta,dq}\boldsymbol{d}_{\alpha\beta,dq} \tag{18}$$

$$\boldsymbol{m}_{\alpha\beta,dq} = \begin{bmatrix} m_{\alpha,d} & m_{\beta,q} \end{bmatrix}^T, \boldsymbol{d}_{\alpha\beta,dq} = \begin{bmatrix} i_{o,\alpha,d} & i_{o,\beta,q} \end{bmatrix}^T \tag{19}$$

The input matrix $\boldsymbol{G}_{\alpha\beta,dq}$, disturbance matrix $\boldsymbol{D}_{\alpha\beta,dq}$, interconnection matrix $\boldsymbol{J}_{\alpha\beta,dq}$ ($\boldsymbol{J}_{\alpha\beta}$ is different from $\boldsymbol{J}_{dq}$), and damping matrix $\boldsymbol{R}_{\alpha\beta,dq}$ are Equation (20).

$$\begin{gathered} \boldsymbol{G}_{\alpha\beta,dq} = \begin{bmatrix} V_{DC} & 0 \\ 0 & V_{DC} \\ 0 & 0 \\ 0 & 0 \end{bmatrix}, \boldsymbol{D}_{\alpha\beta,dq} = \begin{bmatrix} 0 & 0 \\ 0 & 0 \\ -1 & 0 \\ 0 & -1 \end{bmatrix}, \boldsymbol{R}_{\alpha\beta,dq} = \begin{bmatrix} R_{fe} & 0 & 0 & 0 \\ 0 & R_{fe} & 0 & 0 \\ 0 & 0 & 0 & 0 \\ 0 & 0 & 0 & 0 \end{bmatrix}, \boldsymbol{J}_{\alpha\beta} = \begin{bmatrix} 0 & 0 & -1 & 0 \\ 0 & 0 & 0 & -1 \\ 1 & 0 & 0 & 0 \\ 0 & 1 & 0 & 0 \end{bmatrix}, \\ \boldsymbol{J}_{dq} = \begin{bmatrix} 0 & \omega_m & -1 & 0 \\ -\omega_m & 0 & 0 & -1 \\ 1 & 0 & 0 & \omega_m \\ 0 & 1 & -\omega_m & 0 \end{bmatrix} \end{gathered} \tag{20}$$

4. Three-Phase Voltage Source Inverter Controller Design

A passivity-based controller [13–18] was developed using an interconnection and damping assignment (IDA–PBC), which enables the control of a three-phase inverter to be decoupled in the dq frame [27–29]. For the presented inverter model cases, we assume that the coefficients of the matrixes $\boldsymbol{J}_{\alpha\beta,dq}$, $\boldsymbol{R}_{\alpha\beta,dq}$, $\boldsymbol{G}_{\alpha\beta,dq}$, and $\boldsymbol{D}_{\alpha\beta,dq}$ do not depend on the state variables. In an actual inverter, the inductance of L_f can be dependent on the inductor current and switching frequency [36–38].

The controller is designed to follow the reference state variables of the error vector (Equation (21)) in a closed loop system [27].

$$\boldsymbol{e}_{\alpha\beta,dq} = \boldsymbol{x}_{\alpha\beta,dq} - \boldsymbol{x}_{\alpha\beta,dq,ref} \tag{21}$$

The closed loop dynamic (Equation (22)) of the tracking error is described in [27].

$$\dot{\boldsymbol{e}}_{\alpha\beta,dq} = [(\boldsymbol{J}_{\alpha\beta,dq} + \boldsymbol{J}_{\alpha\beta,dq,a}) - (\boldsymbol{R}_{\alpha\beta,dq} + \boldsymbol{R}_{\alpha\beta,dq,a})]\boldsymbol{P}^{-1}\boldsymbol{e}_{\alpha\beta,dq} \tag{22}$$

where:

$$\boldsymbol{P}^{-1}\boldsymbol{e}_{\alpha\beta,dq} = \partial H(\boldsymbol{e}_{\alpha\beta,dq})/\partial \boldsymbol{e}_{\alpha\beta,dq} = \begin{bmatrix} i_{Lf\alpha,d} - i_{Lf\alpha,d,ref} \\ i_{Lf\beta,q} - i_{Lf\beta,q,ref} \\ v_{OUT\alpha,d} - v_{OUT\alpha,d,ref} \\ v_{OUT\beta,q} - v_{OUT\beta,q,ref} \end{bmatrix} \tag{23}$$

The $\boldsymbol{J}_{\alpha\beta,dq,a}$ and $\boldsymbol{R}_{\alpha\beta,dq,a}$ matrices are used to control a closed loop system. The closed loop energy function $H(e_{\alpha\beta,\,dq})$ (Equation (24)) is defined to ensure that the equilibrium is asymptotically stable [36] and will be achieved if $H(e_{\alpha\beta,dq})$ has the minimum in $x_{\alpha\beta,dq,ref}$ (Equation (25)).

$$H(e_{\alpha\beta,dq}) = \frac{1}{2}\boldsymbol{e}_{\alpha\beta,dq}{}^{T}\boldsymbol{P}_{\alpha\beta,dq}{}^{-1}\boldsymbol{e}_{\alpha\beta,dq} \tag{24}$$

$$\left.\frac{\partial H(\boldsymbol{e}_{\alpha\beta,dq})}{\partial \boldsymbol{x}_{\alpha\beta,dq}}\right|_{\boldsymbol{x}_{\alpha\beta,dq,ref}} = 0\ ,\quad \left.\frac{\partial^2 H(\boldsymbol{e}_{\alpha\beta,dq})}{\partial \boldsymbol{x}_{\alpha\beta,dq}{}^{2}}\right|_{\boldsymbol{x}_{\alpha\beta,dq,ref}} > 0 \tag{25}$$

The system is passive if the time derivative $H(e_{\alpha\beta,dq})$ is negative (Equation (26)).

$$\frac{\mathrm{d}H(e_{\alpha\beta,dq})}{\mathrm{d}t} < 0 \tag{26}$$

The requirement (Equation (26)) is met [28] for a positively defined matrix ($\boldsymbol{R}_{\alpha\beta,dq}$ + $\boldsymbol{R}_{\alpha\beta,dq,a}$). The matrix $\boldsymbol{R}_{\alpha\beta,dq,a}$ of injected damping R_i (gain of the current error) and conductance K_v (gain of the voltage error) is defined as Equation (27) and should enable requirement—Equation (26) to be met. As the values of resistance R_i and conductance K_v increase, the speed of tracking error convergence increases but the oscillations of the output voltage can arise (Figure 3).

$$\boldsymbol{R}_{\alpha\beta,dq,a} = \begin{bmatrix} R_i & 0 & 0 & 0 \\ 0 & R_i & 0 & 0 \\ 0 & 0 & K_v & 0 \\ 0 & 0 & 0 & K_v \end{bmatrix} \tag{27}$$

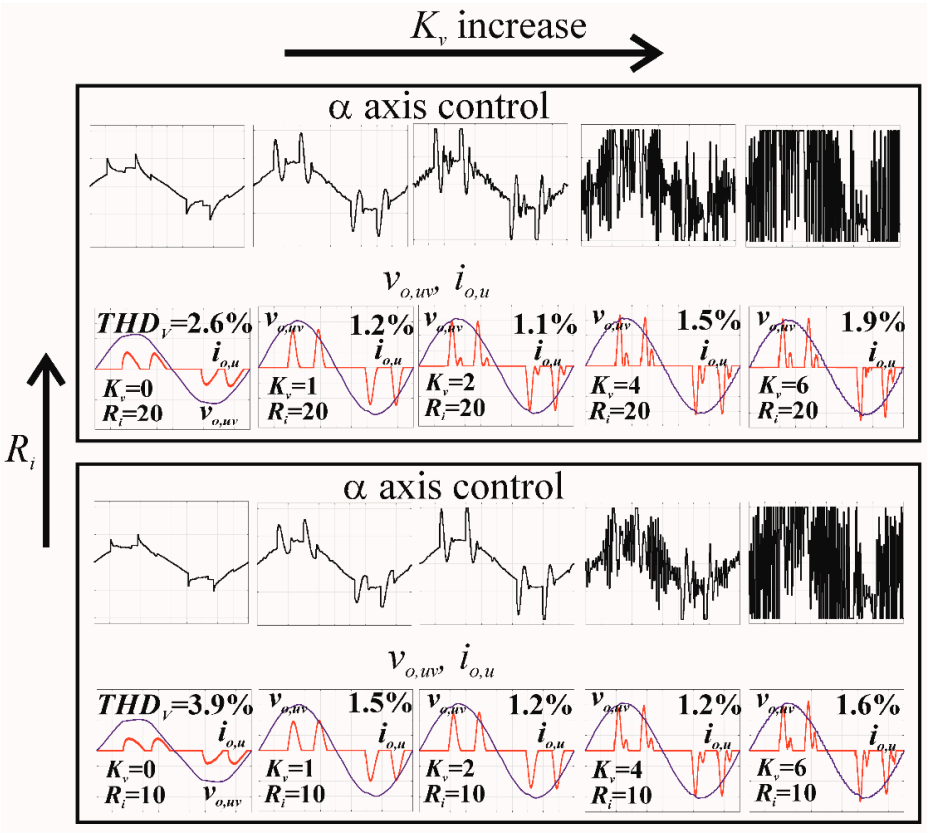

Figure 3. The simulation of the α axis control waveforms, output line-to-line voltages (black), and line currents (red) for the R_i and K_v values (M = 0.3, R_{fe} = 1 Ω, C_f = 50 μF, L_f = 3 mH) for the RC_2 load.

From Equation (26), it is possible to initially define the range of the implemented gains (Equation (28)).

$$R_{fe} + R_i > 0 \text{ and } K_v > 0 \tag{28}$$

In the dq frame, $\boldsymbol{J}_{dq,a}$ should decouple the voltage and current equations from the dq axes (Equations (29) and (30)).

$$\boldsymbol{J}_{dq,a} = \begin{bmatrix} 0 & -\omega_m L_f & 0 & 0 \\ \omega_m L_f & 0 & 0 & 0 \\ 0 & 0 & 0 & -\omega_m C_{fe} \\ 0 & 0 & \omega_m C_{fe} & 0 \end{bmatrix} \tag{29}$$

$$\boldsymbol{J}_{dq} - \boldsymbol{J}_{dq,a} = \begin{bmatrix} 0 & 0 & -1 & 0 \\ 0 & 0 & 0 & -1 \\ 1 & 0 & 0 & 0 \\ 0 & 1 & 0 & 0 \end{bmatrix} = \boldsymbol{J}_{\alpha\beta} \tag{30}$$

In the $\alpha\beta$ frame, $\boldsymbol{J}_{\alpha\beta,a} = 0$ because it is not necessary to decouple the α, β variables.

The roots $\lambda_{1,2}$ (Equation (32)) of the characteristic polynomial (Equation (31)) of a closed loop system (Equation (22)) should be located in the left-half of the s-plane. Theoretically, this will always be fulfilled for the requirement of Equation (28).

$$\det\left\{\left[\left(\boldsymbol{J}_{\alpha\beta,dq} + \boldsymbol{J}_{\alpha\beta,dq,a}\right) - \left(\boldsymbol{R}_{\alpha\beta,dq} + \boldsymbol{R}_{\alpha\beta,dq,a}\right)\right] - \lambda \boldsymbol{I}\right\} = 0 \tag{31}$$

$$\lambda_{1,2} = \frac{\left\{-\left[\left(R_{fe} + R_i\right)C_{fe} + L_f K_v\right] \pm \sqrt{\left[\left(R_{fe} + R_i\right)C_{fe} + L_f K_v\right]^2 - 4L_f C_{fe}\left[1 + \left(R_{fe} + R_i\right)K_v\right]}\right\}}{2L_f C_{fe}} \tag{32}$$

The location of roots $\lambda_{1,2}$ on the complex plane theoretically ensures the stability of the PBC system. However, Figure 3 presents the simulations of the $v_{o,uv}$ line-to-line voltage, the $i_{o,u}$ line current and the α axis control waveform for $R_{fe} = 1\ \Omega$, $C_f = 50\ \mu\text{F}$, $L_f = 3\ \text{mH}$ and the inverter nonlinear rectifier RC_2 load ($R_{load} = 47\ \Omega$, $C_{load} = 470\ \mu\text{F}$) for PBC in the stationary $\alpha\beta$frame. The modulation index was set at $M = 0.3$. The lower value of M would give better results of control [32] but would be completely unrealistic. Figure 3 shows that for $K_v = 0$ (the basic PBC), the output voltage error amplification is too low for $R_i = 10\ \Omega$ or $20\ \Omega$ and the THD_v coefficient is high and for the $K_v > 2\ \Omega^{-1}$ for $R_i = 10\ \Omega$ or $R_i = 20\ \Omega$, there are oscillations of the αaxis control waveform, which results in the oscillations of the output voltage. The saturation of the αaxis control waveform for $K_v R_i > 40$ inhibits the further reduction of output voltage distortions. For further simulations for both controllers, Improved PBC v.2 (IPBC2) and IDA–PBC, $M = 0.3$, $R_i = 10\ \Omega$ and $K_v = 2\ \Omega^{-1}$ were selected because of the relatively low THD_v, the lack of control oscillations, and the lack of any αaxis control waveform saturation. The control law (Equation (33)) was determined in the $\alpha\beta$frame (Equations (34) and (35)) and the dq frame (Equations (36)–(39)) by subtracting both sides of the Equations (16) for the $\alpha\beta$frame or Equation (23) for the dq frame from both sides of Equation (28).

$$\begin{aligned} \boldsymbol{G}_{\alpha\beta,dq}\boldsymbol{m}_{\alpha\beta,dq} = \; & -\left[\boldsymbol{J}_{\alpha\beta,dq} - \boldsymbol{R}_{\alpha\beta,dq}\right]\boldsymbol{P}_{\alpha\beta,dq}{}^{-1}\boldsymbol{x}_{\alpha\beta,dq,ref} + \left[\boldsymbol{J}_{\alpha\beta,dq,a} - \boldsymbol{R}_{\alpha\beta,dq,a}\right]\boldsymbol{P}_{\alpha\beta,dq}{}^{-1}\left(\boldsymbol{x}_{\alpha\beta,dq} - \boldsymbol{x}_{\alpha\beta,dq,ref}\right) - \\ & -\boldsymbol{D}_{\alpha\beta,dq}\boldsymbol{d}_{\alpha\beta,dq} + \dot{\boldsymbol{x}}_{\alpha\beta,dq,ref} \end{aligned} \tag{33}$$

The difference control law for the stationary $\alpha\beta$ frame (Equations (34) and (35)) for $K_v = 0$ is the same as the control law for the conventional PBC [22]. Introducing K_v (control of the output voltage error) makes the control law similar to the IPBC from [22]. However, the addition of the derivative

of the output voltage error in the final control law should enable the dynamic changes in the output voltage to be reduced faster. This type of PBC will further be called IPBC2.

$$\begin{aligned} V_{CTRL,\alpha,\beta}(k) &= L_f[i_{Lf,\alpha,\beta,ref}(k) - i_{Lf,\alpha,\beta,ref}(k-1)]f_s + R_{fe}i_{Lf,\alpha,\beta,ref}(k) - \\ &-R_i[i_{Lf,\alpha,\beta}(k) - i_{Lf,\alpha,\beta,ref}(k)] + v_{o,\alpha,\beta,ref}(k) \end{aligned} \tag{34}$$

here the reference inductor current $i_{Lf,\alpha,\beta,ref}$ is (35).

$$i_{Lf,\alpha,\beta,ref}(k) = C_{fe}[v_{o,\alpha,\beta,ref}(k) - v_{o,\alpha,\beta,ref}(k-1)]f_s - K_v[v_{o,\alpha,\beta}(k) - v_{o,\alpha,\beta,ref}(k)] + i_{o,\alpha,\beta}(k) \tag{35}$$

The difference control law of IDA–PBC [27] for the rotating dq frame is Equations (36)–(39).

$$\begin{aligned} V_{CTRL,d}(k) &= L_f[i_{Lf,d,ref}(k) - i_{Lf,d,ref}(k-1)]f_s + R_{fe}i_{Lf,d,ref}(k) - \omega_{dq}L_f i_{Lf,q} - \\ &-R_i[i_{Lf,d}(k) - i_{Lf,d,ref}(k)] + v_{o,d,ref}(k) \end{aligned} \tag{36}$$

$$i_{Lf,d,ref}(k) = C_{fe}[v_{o,d,ref}(k) - v_{o,d,ref}(k-1)]f_s - \omega_{dq}C_{fe}v_{o,q} - K_v[v_{o,d}(k) - v_{o,d,ref}(k)] + i_{o,d}(k) \tag{37}$$

$$\begin{aligned} V_{CTRL,q}(k) &= L_f[i_{Lf,q,ref}(k) - i_{Lf,q,ref}(k-1)]f_s + R_{fe}i_{Lf,q,ref}(k) + \omega_{dq}L_f i_{Lf,d} - \\ &-R_i[i_{Lf,q}(k) - i_{Lf,q,ref}(k)] + v_{o,q,ref}(k) \end{aligned} \tag{38}$$

$$i_{Lf,q,ref}(k) = C_{fe}[v_{o,q,ref}(k) - v_{o,q,ref}(k-1)]f_s + \omega_{dq}C_{fe}v_{o,d} - K_v[v_{o,q}(k) - v_{o,q,ref}(k)] + i_{o,q}(k) \tag{39}$$

For a three-phase AC power supply in the $\alpha\beta$ frame, the difference of reference voltage $v_{o,\alpha,\beta,ref}(k) - v_{o,\alpha,\beta,ref}(k-1) \neq 0$ because $v_{o,\alpha,\beta,ref}$ are two shifted values with $\pi/2$ sinusoidal waveforms. For the dq frame, $v_{o,d,q,ref}(k) - v_{o,d,q,ref}(k-1) = 0$ because $v_{o,d,q,ref}$ are two constant values.

5. Modeling and Measurement of a Three-Phase Inverter with IPBC2 and IDA–PBC Control for Standard Loads

The calculations of IPBC2 in the stationary $\alpha\beta$ frame using only the Clarke transformation without any interactions and without the angular speed ω_m as additional input are faster than the calculations of IDA–PBC [27] in the rotating dq frame. Both control systems were initially tested using the simulation models in MATLAB–Simulink and are implemented in the experimental model that was controlled with an STM32F407VG microprocessor. The switching frequency was f_s = 12,800 Hz (256 switching periods in one fundamental period). For f_s = 12,800 Hz, we have less than 78 µs for measuring three output voltages, three output currents, and three inductor currents (there are three independent Analog-to-Digital Converters (ADC)) in a three-phase inverter, calculating three Clarke transformations and executing the control laws for PBC in the stationary frame and the reverse Clarke transformations. In IDA–PBC we should additionally calculate three Park transformations and three reverse Park transformations. The whole microprocessor program is based on PWM interrupts that call ADC conversions. The first and the second ADC interrupts after a conversion is finished call the next ADC conversion, the third ADC interrupt calls the subroutines with the Clark and Park transformations (only for IDA–PBC), calculates the control laws, reverses Clark and Park transformations, and finally the results of the calculations are stored in the three registers of PWM comparators, which will change the output pulse width in the next switching period. We can easily check that all of these activities do not exceed 78 µs—the lower priority interrupts and the main loop procedures should be available and executed.

The dynamic delta load that was tested was Δ470 Ω switched to Δ470||47 Ω and vice versa. The nonlinear rectifier RC_1 load (C_{load} = 100 µF, R_{load} = 47 Ω) or RC_2 load (C_{load} = 470 µF, R_{load} = 47 Ω) was used. The measured value [37] of the coil inductance with a Material Mix -26 iron-powder core [37] in the operating point was approximately L_f = 3 mH and R_{fe} = 1 Ω due to the power losses in the core [36,38]. For the delta load, $C_{fe} = 3C_f$ = 150 µF. Modeling in MATLAB–Simulink does not solve some of the serious problems with separate scaling voltages and currents. In an actual inverter, the nominal values of the voltage and current have to be amplified to achieve approximately 2/3 of the maximum

value of the analogue to digital converter (ADC) range (for 12-bit ADC the range is 0–4095) because we have to predict the instantaneous increase in the nominal value (e.g., for a step decrease of the load). The other problem is how to limit the maximum value of the control voltage in the input of the PWM modulator (the output value of the control law). In the presented actual inverter, the limit was ±3280 (for an input PWM modulator frequency of 84 MHz and a switching frequency f_s = 12,800 Hz). In the MATLAB–Simulink model, it was ±1 (Figure 3). The actual delays and phase shifts of the filters that were used can only be measured in the device. During switching instants, there are spikes in the measured voltage waveforms and a voltage amplifier with the galvanic isolation can introduce a noise. The additional low pass filter (an anti-aliasing filter can be insufficient) can be an effective solution. These problems are absent in the MATLAB–Simulink model. The control signal should suppress the distortions of the output voltage. A similar analysis as for the simulation in Figure 3 was performed for the experimental model with IPBC2 and is partly presented in Figure 4a–d. Figure 4a–d presents the visualization—digital to analogue conversion of the digital PWM α axis control signal for the IPBC2 control in the experimental model for the control parameters that were finally selected: R_i = 15 Ω, K_v = 0.8 Ω^{-1} for M = 0.3 (Table 1). Figure 4d shows the control signal saturation that resulted in a decreased control quality when compared with Figure 4c. The different values of parameters R_i and K_v for the experimental model and the simulation were caused by the current and voltage scaling factors in the experimental model. The three-phase inverter MATLAB–Simulink simulation results were compared with the experimental model measurements for the open loop, IPBC2, and IDA–PBC controllers. The actual measured [36] values of the filter parameters were used. In the experimental model for IPBC2: R_i = 15 Ω, K_v = 0.8 Ω^{-1}, M = 0.3, for IDA–PBC: R_i = 18 Ω, K_v = 0.5 Ω^{-1}, M = 0.3 (Table 1). Further increasing R_i and K_v caused some oscillations in the output voltages.

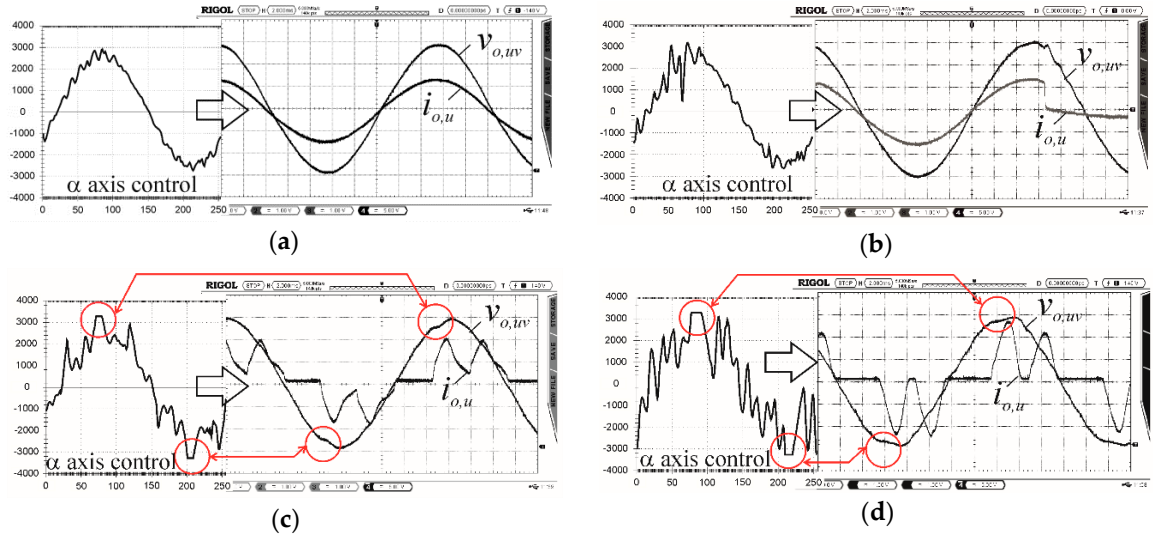

Figure 4. Control waveforms in the α axis for IPBC2 (M = 0.3, R_i = 15, K_v = 0.8, L_f = 3 mH, C_f = 50 μF) of the experimental inverter and output line-to-line voltage $v_{o,uv}$ vs. line current $i_{o,u}$ for: (**a**) static linear load Δ47 Ω, (**b**) dynamic load, (**c**) rectifier RC_1 load, (**d**) rectifier RC_2 load.

Table 1. Parameters of the simulation model and the inverter experimental models.

Type of the Model	L_f (mH)	R_{fe} (Ω)	C_f (μF)	M	$V_{o,uv}\|_{max}$ (V)	R_i (Ω)	K_v (Ω^{-1})
MATLAB Simulation	3	1	50	0.3	150	10	2
Experimental IPBC2	3	1	50	0.3	70	15	0.8
Experimental IDA–PBC	3	1	50	0.3	70	18	0.5

Figure 5a–c, Figure 6a–c, Figure 7a–c, Figure 8a–c, Figure 9a–c, and Figure 10a–c are the simulations and measurements of the three-phase VSI with the open feedback loop, with the IPBC2 ($\alpha\beta$ frame),

with the IDA–IPBC (*dq* frame), for the dynamic three-wire delta load, and the nonlinear rectifier RC_1 and RC_2 loads, respectively. The simulations and measurements gave very similar results for the open feedback loop, which verified the simulation model.

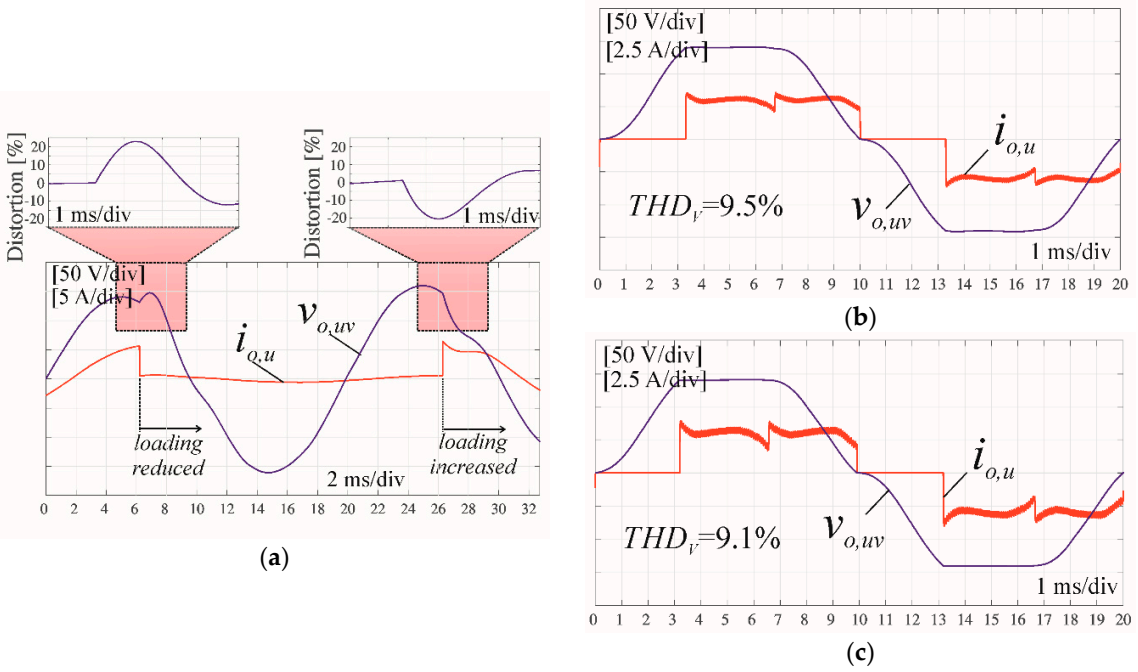

Figure 5. Simulations of the open loop three-phase inverter for a three-wire load: (**a**) dynamic resistive load, (**b**) rectifier RC_1 load, (**c**) rectifier RC_2 load.

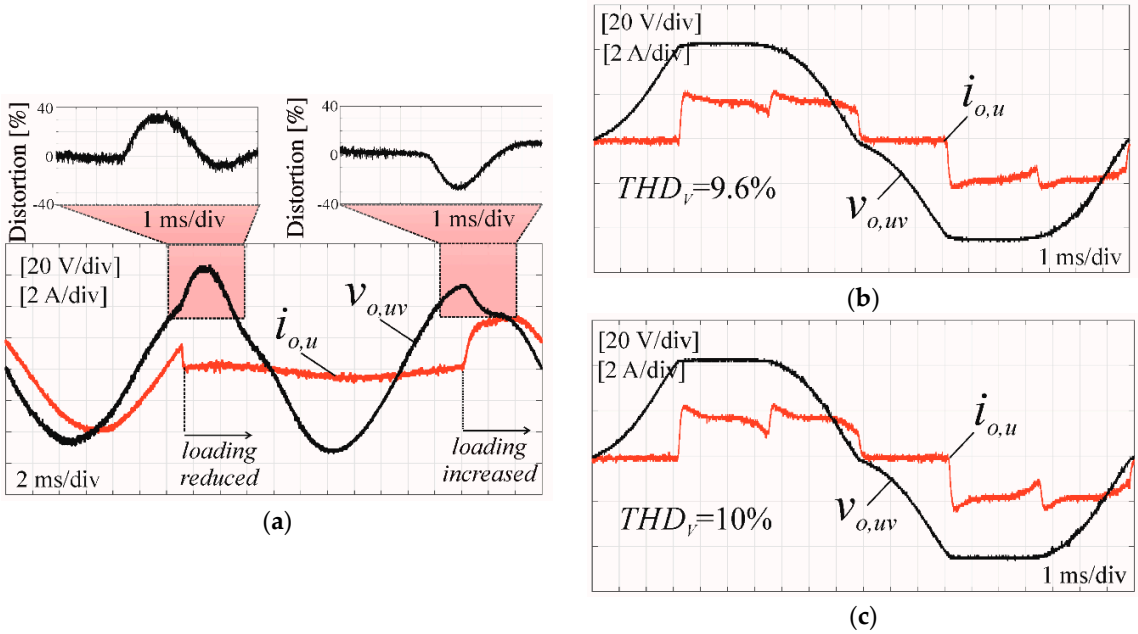

Figure 6. Measurements of the open loop three-phase inverter for a three-wire load: (**a**) dynamic resistive load, (**b**) rectifier RC_1 load, (**c**) rectifier RC_2 load.

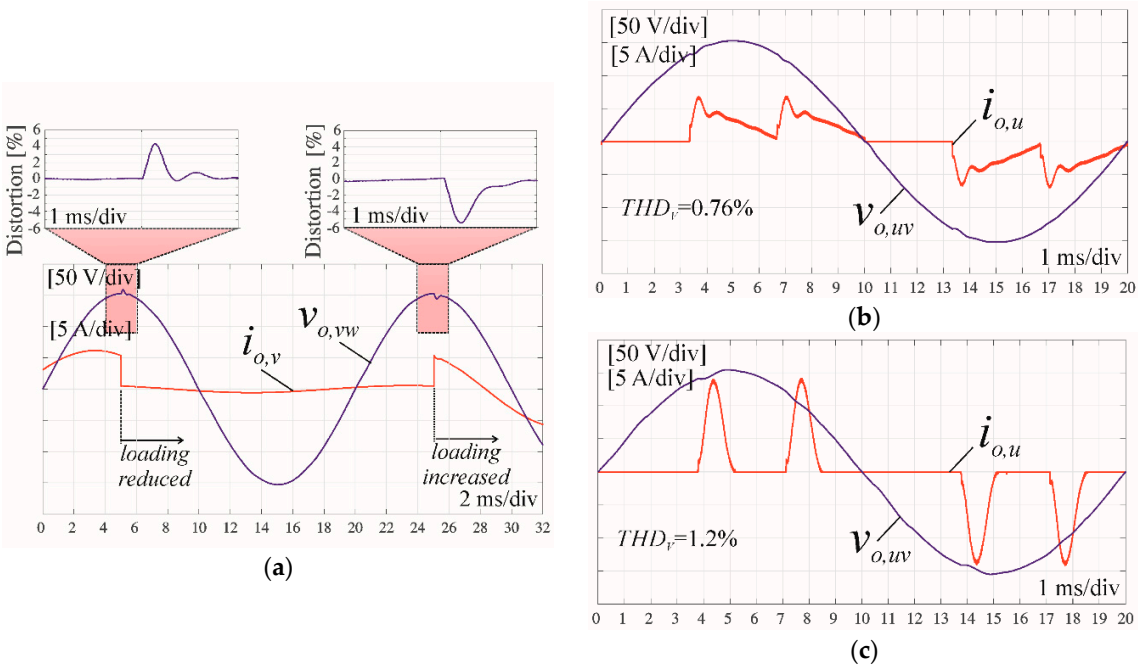

Figure 7. Simulations of the open loop three-phase inverter with IPBC2 (using the stationary $\alpha\beta$ frame, $M = 0.3$, $R_i = 10\ \Omega$, $K_v = 2\ \Omega^{-1}$): (**a**) dynamic resistive load, (**b**) rectifier RC_1 load, (**c**) rectifier RC_2 load.

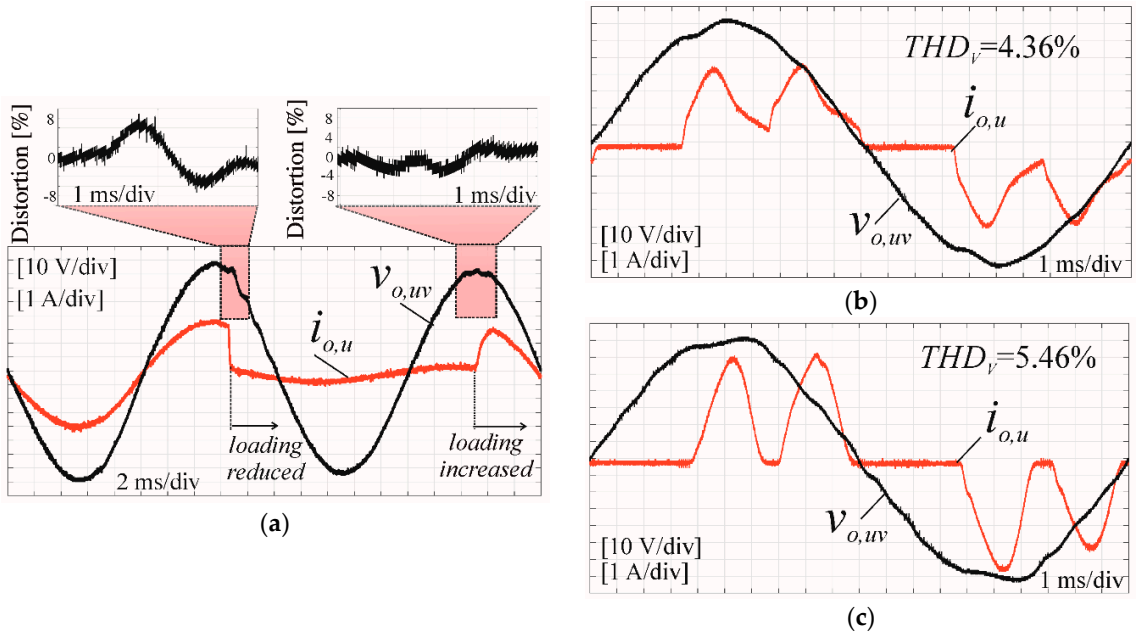

Figure 8. Measurements of the three-phase experimental inverter with IPBC2 for a three-wire load (using the stationary αβ frame, $M = 0.3$, $R_i = 15\ \Omega$, $K_v = 0.8\ \Omega^{-1}$): (**a**) dynamic resistive load, (**b**) rectifier RC_1 load, (**c**) rectifier RC_2 load.

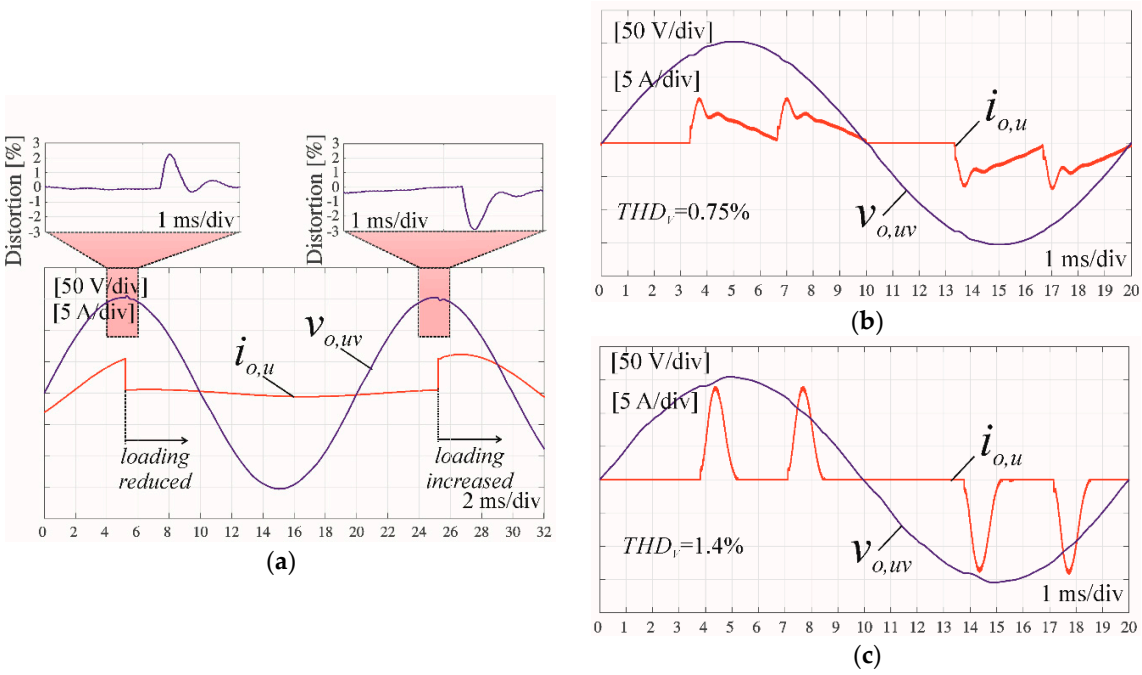

Figure 9. Simulations of the three-phase inverter with IDA–PBC (using the rotating *dq* frame, $M = 0.3$, $R_i = 10\ \Omega$, $K_v = 2\ \Omega^{-1}$): (**a**) dynamic resistive load, (**b**) rectifier RC_1 load, (**c**) rectifier RC_2 load.

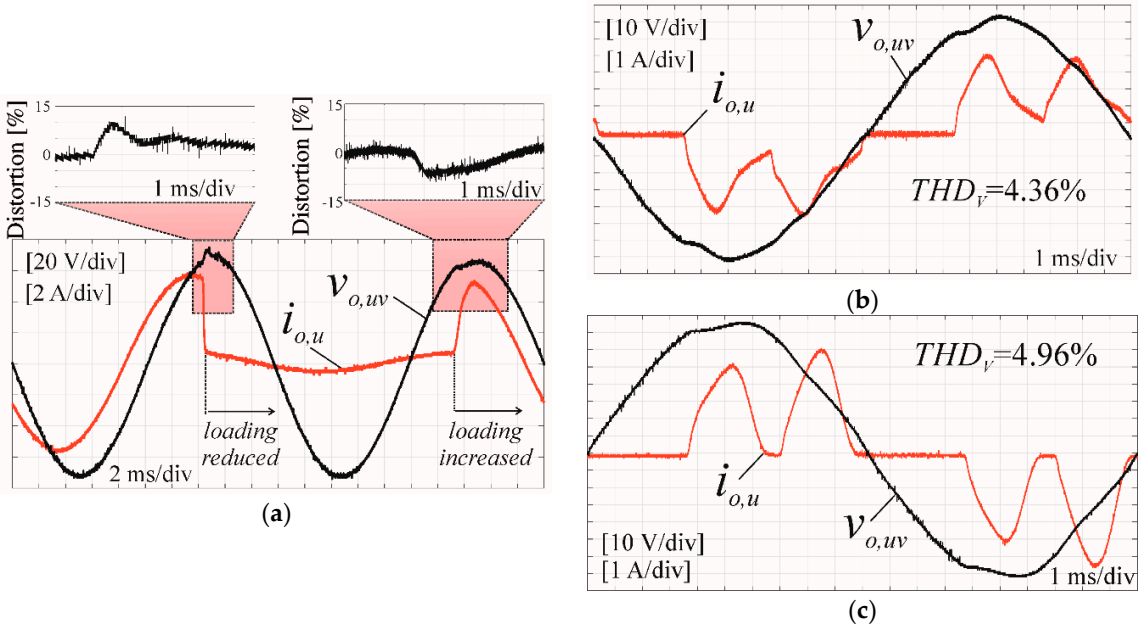

Figure 10. Measurements of the three-phase experimental inverter with IDA–PBC for a three-wire load (using the rotating *dq* frame, $M = 0.3$, $R_i = 18$, $K_v = 0.5$): (**a**) dynamic resistive load, (**b**) rectifier RC_1 load, (**c**) rectifier RC_2 load.

The presented simulations and measurements (Table 2) show that using different versions of PBC, the overshoot or undershoot for the step load was reduced in the experimental model from ±30% to ±5–±10% and the THD_V was decreased from 10% to about 4–5% (in the simulations to 1%). The reasons for the different results of the simulations and measurements are discussed in the results. Both control systems, IPBC2 and IDA–PBC, gave similar results.

Table 2. Results of the simulations and the measurements of the inverter experimental model.

	R_i (Ω)	K_v (Ω^{-1})	THD_V RC_1	THD_V RC_2	Overshoot Load Decrease	Undershoot Load Increase
No feedback. simulation	—	—	9.5%	9.1%	+23%	−20%
No feedback inverter	—	—	9.6%	10%	+32%	−28%
IPBC2 simulation	10	2	0.76%	1.2%	+4.5%	−5.5%
IPBC2 inverter	15	0.8	4.36%	5.46%	+7%	−4%
IDA–PBC simulation	10	2	0.75%	1.4%	+2.2%	−3%
IDA–PBC inverter	18	0.5	3.93%	4.96%	+10%	−7%

6. Results

6.1. Modulation Index Choice

The most important problem is the limitation of the input/output range of the modulator signals (Figures 3 and 4c,d). This is one reason for the greater distortions of the output voltage in the experimental inverter than in the simulations. An excessive increase of the controller gains causes the saturation of the control signal and oscillations of the output voltage (the imaginary part of the roots of the characteristic equation of the closed loop system increases with the gain, Figure 3). Therefore, one of the most important problems in inverter control is maintaining a sufficient range for the possible changes in the input voltage of a PWM modulator. For a lower M modulation index, this range increases. However, using a very low value, e.g., $M = 0.3$, is not permissible for actual inverters. The compromise between the high (close to the unity) modulation index M that is used in actual inverters and the low M that enables a sufficient control dynamic depending on the value of the inductors in the output filter is required.

6.2. Controller Gains Adjustment

To design the control (IPBC2) of an inverter (Figure 11), we should test the output voltage for the selected nonlinear rectifier RC load for the assigned M modulation index and for the wide spectrum of gains $R_i > 0$ and $K_v \geq 0$ and measure the THD_V coefficient. For low values of these parameters, we will receive high values of THD_V. We should increase R_i and K_v (the exemplary values are in Table 2). For $K_v > 0$, at first the THD_V coefficient decreases, it reaches the minimum, and then it increases. After crossing the minimum of THD_V, the oscillations will appear in the output voltage and the control signal can become saturated. Close to the minimum of the THD_V coefficient, we can designate the values of the parameters R_i and K_v (separately for the simulation and the experimental model) to avoid output voltage oscillations and the control signal waveform saturation (Figure 3, Figure 4, and Figure 11). A lower value of the gain K_v in the experimental inverter was selected (Figure 4) than in the simulation (Figure 11) because there are output voltage and current scaling factors in the experimental inverter that can change the effective gain.

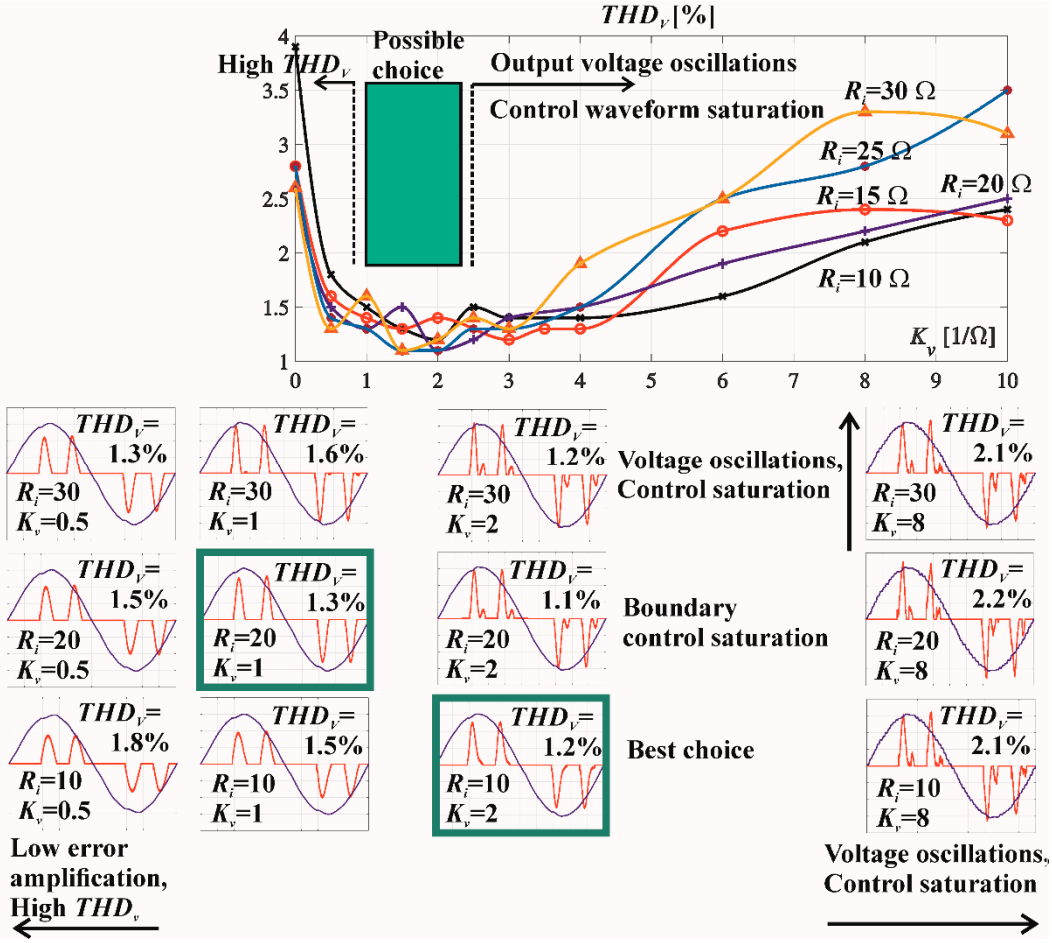

Figure 11. The selection of the acceptable parameters R_i and K_v (IPBC2) based on the analysis of the THD_v of the output inverter line-to-line voltage $v_{o,uv}$ (blue) and the line current $i_{o,u}$ (red) for the nonlinear rectifier RC_2 load—the simulation.

6.3. Differences Between Results of the Simulation and the Experimental Inverter Measurements

The simulation results were better than the experimental inverter (Figure 12) measurements (lower overshoot and undershoot, lower THD_V of the output voltage for the rectifier RC load in IPBC2 and IDA–PBC controls), possibly because the selected scaling factors of the voltages and currents were imperfect. The saturation of the control signal had different levels in the simulations and in the experimental model; we always had a problem with the value of the modulation index versus the inductance of the filter coil (Equation (3)), which can inhibit the effective reduction of the output voltage distortions. The simulated voltages had higher amplitude than those in the experimental model and the ripple voltage in the simulations can cause a lower effect of THD_V (THD_V was lower for the simulations). The actual parameters of components of an inverter output filter in the operation point can be different from the nominal values [36,38], which can increase the differences between the simulations and theory.

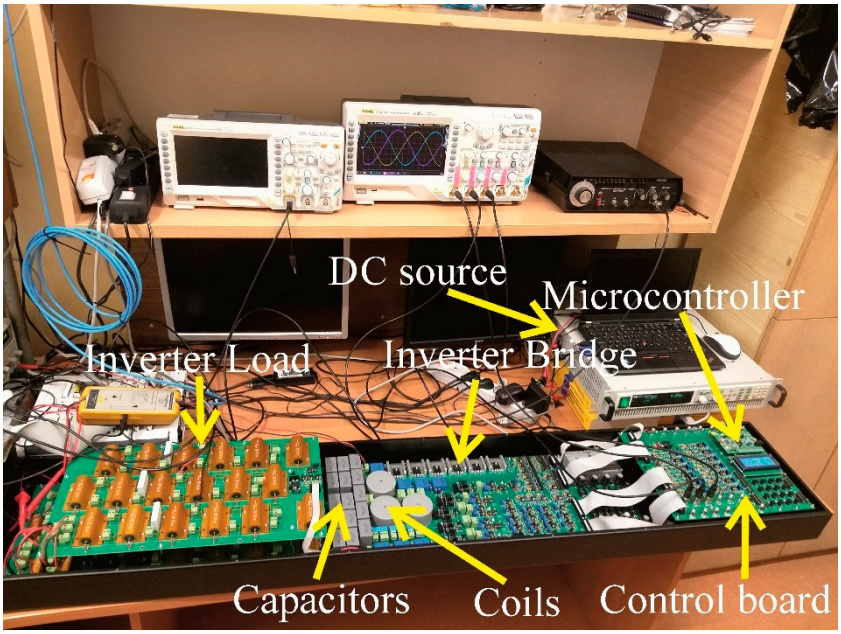

Figure 12. Experimental model.

6.4. Advantages of the Control in the Stationary Frame

Both IPBC2 and IDA–PBC that are described are based on the same state equations of the inverter. IPBC2 is described in the stationary $\alpha\beta$ frame and the control laws in α and β axes are fully decoupled. This idea can easily be implemented in single-phase inverters, e.g., for efficiently decreasing the output voltage distortions of the Z-Source inverter [39]. The stationary $\alpha\beta$ frame can be transformed to the rotating dq frame that implements the interconnections from one axis to the other. The idea of IDA–PBC control is simply to remove them. IDA–PBC requires many more calculations for the Park transformation but its constant reference values are its advantage. The results of using both control systems in a VSI are the same. Therefore, it is better to use the easier calculations in IPBC2 without the Park transformation.

6.5. The Steady-State Error Reduction

It seems that the control laws of IDA–PBC and IPBC2 do not include any direct integration of the output voltage error, which is a rather PD-like control of the output voltage. However, the control law considers the filter inductor current, which depends on integrating the voltage on the inductor, and thus indirectly on the inverter output voltage. In the classic PBC control versions that are presented in [22], there is no direct control of the output voltage at all. The output impedance of the inverter with the open control loop (without the transformer increasing voltage) is rather low. It can be calculated from the measurements that are presented in Figure 6a. In Figure 10a, the steady-state error in the inverter with IDA–PBC is close to zero.

7. Discussion

The presented PBC control has been widely presented in the literature [13–18,22,24,35]. The paper shows that simple calculations without decoupling in the three-phase control in the $\alpha\beta$ frame result in similar distortions of the inverter output voltage as the control in the dq frame that requires more calculations and additional decoupling [27]. The paper focuses on the fact that quality of the inverter output voltage for the standard loads depends on parameters such as the modulation index [32], the saturation of the control signal, and taking in account the delay of the control system, the values of the output filter parameters, and their variability [36,38]. The paper presents the idea of initially adjusting the parameters (using simulations) of the improved PBC controller. Further research should

enable the analytic calculations of the parameters of the PBC controller. This is important because the improved (with the direct control of the inverter output voltage) PBC seems be perfect for systems that convert energy such as e.g., inverters.

8. Conclusions

The output filter parameters can be initially calculated to achieve a low output voltage ripple in a steady state operation. However, the capacitance should be increased due to the output voltage increase during a switching period in cases where the load current decreases steeply and all of the inductor current flows through the filter capacitor. It was shown that both control systems, IPBC2 (using the stationary $\alpha\beta$ frame) and IDA–PBC (using the rotating dq frame), resulted in a similar decrease in the distortions in the three-phase inverter output voltage. Therefore, for a constant frequency of the reference waveform, it is better to use IPBC2 without the Park and reverse Park transformations. The demands concerning the microprocessor that controls the system are lower when we use a stationary frame. The real quality of the output voltage depends on the maximum range of the PWM driver control signals. Lower M modulation indices result in better control results because it is possible to omit the controller saturation for the less restricted range of controller gains. However, this approach cannot be used in commercial designs where the modulation index is close to unity to fully utilize the input DC power source. The other restriction of the control results is that too large a value of the inductance in the output filter makes the current changes slower than required. It is clear that the product $M_{max}L_{fe}$ should be limited. The simulations that were necessary before experimental tests have a significant disadvantage—they do not solve the problem of voltage and current measurement scaling. Moreover, the scaling coefficients are as important as the gains in the control law. The paper shows an easy way to adjust the controller gains (Figures 3 and 11). These gains in IPBC2 had a wide margin of tolerance.

Author Contributions: Conceptualization, Z.R. and K.B.; methodology, Z.R. and K.B.; software, Z.R.; validation, Z.R., K.B. and Ł.D.; formal analysis, Z.R., K.B., Ł.D. and P.D.; investigation, Z.R. and K.B.; resources, Z.R. and K.B.; Writing—Original draft preparation, Z.R.; Writing—Review and editing, Z.R., K.B., Ł.D. and P.D.; visualization, Z.R. and P.D.; supervision, Z.R.; project administration, Z.R. and K.B.; funding acquisition, Z.R., K.B. and Ł.D.

Funding: This research was partially supported by the Polish Ministry of Science and Higher Education funding for statutory activities. Authors were supported by the Polish National Centre for Research and Development, grant no. TANGO3/427467/NCBR/2019.

Acknowledgments: The calculations were performed using the IT infrastructure that was funded by the GeCONiI project (POIG.02.03.01-24-099/13).

Conflicts of Interest: The authors declare no conflict of interest.

References

1. Ben-Brahim, L.; Yokoyama, T.; Kawamura, A. Digital control for UPS inverters. In Proceedings of the Fifth International Conference on Power Electronics and Drive Systems, Singapore, 17–20 November 2003; pp. 1252–1257.
2. Kawamura, A.; Yokoyama, T. Comparison of five different approaches for real time digital feedback control of PWM inverters. In Proceedings of the IEEE Industry Applied Society Annual Meeting, Seattle, WA, USA, 7–12 October 1990; pp. 1005–1011.
3. Luo, F.L.; Ye, H.; Rashid, M. *Digital Power Electronics and Applications*; Elsevier Academic Press: San Diego, CA, USA, 2010.
4. Rech, C.; Pinheiro, H.; Grundling, H.A.; Hey, H.L.; Pinheiro, J.R. Comparison of Digital Control Techniques with Repetitive Integral Action for Low Cost PWM Inverters. *IEEE Trans. Power Electron.* **2003**, *18*, 401–410. [CrossRef]
5. Sangwongwanich, A.; Abdelhakim, A.; Yangand, Y.; Zhou, K. Control of Single-Phase and Three-Phase DC/AC Converters. In *Control of Power Electronic Converters and Systems*; Blaabjerg, F., Ed.; Elsevier Academic Press: London, UK, 2018; Volume 6, pp. 153–172.

6. Zou, Z.X.; Wang, Z.; Cheng, M. Design and analysis of operating strategies for a generalised voltage-source power supply based on internal model principle. *IET Power Electron.* **2014**, *7*, 330–339. [CrossRef]
7. Gui, Y.; Wei, B.; Li, M.; Guerrero, J.M.; Vasquez, J.C. Passivity-based coordinated control for islanded AC microgrid. *Appl. Energy* **2018**, *229*, 551–561. [CrossRef]
8. Uninterruptible Power Systems (UPS)—Part 3: Method of Specifying the Performance and Test Requirements. Available online: https://webstore.iec.ch/publication/6344 (accessed on 10 October 2019).
9. Blachuta, M.; Rymarski, Z.; Bieda, R.; Bernacki, K.; Grygiel, R. Design, Modeling and Simulation of PID Control for DC/AC Inverters. In Proceedings of the 24th International Conference on Methods and Models in Automation and Robotics, Międzyzdroje, Poland, 26–29 August 2019; pp. 428–433.
10. Manabe, S. Importance of coefficient diagram in polynomial method. In Proceedings of the 42nd IEEE Conference on Decision and Control, Maui, HI, USA, 9–12 December 2003; pp. 3489–3494.
11. Zhao, G.; Miao, G.; Yong, W. Application of Repetitive Control for Aeronautical Static Inverter. In Proceedings of the 2nd IEEE Conference on Industrial Electronics and Applications, Harbin, China, 23–25 May 2007; pp. 121–125.
12. Rymarski, Z. Design method of single-phase inverters for UPS systems. *Int. J. Electron.* **2009**, *96*, 521–535. [CrossRef]
13. Ortega, R.; Spong, M.W. Adaptive motion control of rigid robots: A tutorial. *Automatica* **1989**, *25*, 877–888. [CrossRef]
14. Ortega, R.; Perez, J.A.L.; Nicklasson, P.J.; Sira-Ramirez, H.J.; Sira-Ramirez, H. *Passivity-Based Control of Euler-Lagrange Systems: Mechanical, Electrical and Electromechanical Applications (Communications and Control Engineering)*; Springer: London, UK, 1998.
15. Ortega, R.; Garcia-Canseco, E. Interconnection and Damping Assignment Passivity-Based Control: A Survey. *Eur. J. Control* **2004**, *5*, 432–450. [CrossRef]
16. Ortega, R.; Garcia-Canseco, E. Interconnection and Damping Assignment Passivity-Based Control: Towards a Constructive Procedure—Part I. In Proceedings of the 43rd IEEE Conference on Decision and Control, Nassau, Bahamas, 14–17 December 2004; pp. 3412–3417.
17. Ortega, R.; Espinosa-Perez, G. Passivity-based control with simultaneous energy-shaping and damping injection: The induction motor case study. *IFAC Proc. Vol.* **2005**, *38*, 477–482. [CrossRef]
18. Torres, M.; Ortega, R. Feedback Linearization, Integrator Backstepping and Passivity-Based Controller Designs: A Comparison Example. In *Perspectives in Control. Theory and Applications*; Normand-Cyrot, D., Ed.; Springer: London, UK, 1998.
19. Wang, W.J.; Chen, J.Y. Compositive adaptive position control of induction motors based on passivity theory. *IEEE Trans. Energy Convers.* **2001**, *16*, 180–185. [CrossRef]
20. Wang, W.J.; Chen, J.Y. Passivity-based sliding mode position control for induction motor drives. *IEEE Trans. Energy Convers.* **2005**, *20*, 316–321. [CrossRef]
21. Hill, D.; Zhao, J.; Gregg, R.; Ortega, R. 20 Years of Passivity-Based Control (PBC): Theory and Applications. In Proceedings of the CDC Workshop, Shanghai, China, 15 December 2009; pp. 1–85.
22. Komurcugil, H. Improved passivity-based control method and its robustness analysis for single-phase uninterruptible power supply inverters. *IET Power Electron.* **2015**, *8*, 1558–1570. [CrossRef]
23. Jie, B.; Lee, P.L. Passivity-based Robust Control. In *Advances in Industrial Control*; Springer: London, UK, 2007; pp. 43–88.
24. Bu, N.; Deng, M.C. Passivity-based robust control for uncertain nonlinear feedback systems. *J. Robot. Mechatron.* **2016**, *28*, 837–841. [CrossRef]
25. Rymarski, Z.; Bernacki, K.; Dyga, Ł. A control for an unbalanced 3-phase load in UPS systems. *Elektronika Ir Elektrotechnika* **2018**, *24*, 27–31. [CrossRef]
26. Available online: https://iris.unicampania.it/handle/11591/178750#.XcZk89URXIV (accessed on 10 October 2019).
27. Serra, F.M.; De Angelo, C.H.; Forchetti, D.G. IDA-PBC control of a DC-AC converter for sinusoidal three-phase voltage generation. *Int. J. Electron.* **2017**, *104*, 93–110. [CrossRef]
28. Khefifi, N.; Houari, A.; Ait-Ahmed, M.; Machmoum, M.; Ghanes, M. Robust IDA-PBC based Load Voltage Controller for Power Quality Enhancement of Standalone Microgrids. In Proceedings of the IEEE IECON 2018—44th Annual Conference of the IEEE Industrial Electronics Society, Washington, DC, USA, 21–23 October 2018; pp. 249–254.

29. Meshram, R.V.; Bhagwat, M.; Khade, S.; Wagh, S.R.; Aleksandar, M.; Stankovic, A.M.; Singh, N.M. Port-Controlled Phasor Hamiltonian Modeling and IDA-PBC Control of Solid-State Transformer. *IEEE Trans. Control Syst. Technol.* **2019**, *27*, 161–174. [CrossRef]
30. Dahono, P.A.; Purwadi, A.; Qamaruzzaman. An LC filter design method for single-phase PWM inverters. In Proceedings of the International Conference on Power Electronics and Drive System, Singapore, 21–24 February 1995; pp. 571–576.
31. Rymarski, Z. The discrete model of power stage of the voltage source inverter for UPS. *Int. J. Electron.* **2001**, *98*, 1291–1304. [CrossRef]
32. Rymarski, Z. The analysis of output voltage distortion minimization in the 3-phase VSI for the nonlinear rectifier R_OC_O load. *Przegląd Elektrotechniczny (Electr. Rev.)* **2009**, *85*, 127–132.
33. Chattopadhyay, S.; Mitra, M.; Sengupta, S. *Electric Power Quality*; Springer: Dordrecht, The Netherlands, 2013.
34. Akagi, H.; Watanabe, E.H.; Aredes, M. *Instanteneous Power Theory and Application to Power Conditionig, In IEEE Press Series on Power Engineering*; Willey-Interscience, Willey and Sons, Inc.: Hoboken, NJ, USA, 2007.
35. Wang, Z.; Goldsmith, P. Modified energy-balancing-based control for the tracking problem. *IET Control Theory Appl.* **2008**, *2*, 310–312. [CrossRef]
36. Rymarski, Z. Measuring the real parameters of single-phase voltage source inverters for UPS systems. *Int. J. Electron.* **2017**, *104*, 1020–1033. [CrossRef]
37. 2019 Iron Powder Products Catalog. Available online: https://micrometals.com (accessed on 24 September 2019).
38. Bernacki, K.; Rymarski, Z.; Dyga, Ł. Selecting the coil core powder material for the output filter of a voltage source inverter. *IET Electron.* **2017**, *53*, 1068–1069. [CrossRef]
39. Rymarski, Z.; Bernacki, K.; Dyga, Ł. Decreasing the single phase inverter output voltage distortions caused by impedance networks. *IEEE Trans. Ind. Appl.* **2019**. [CrossRef]